Electronic Supplementary Material (ESI) for Physical Chemistry Chemical Physics.

Enhanced Intermediate-Temperature CO_2 Splitting Using Nonstoichiometric Ceria and Ceria-Zirconia

Zhenlong Zhao [a], Mruthunjaya Uddi [b], Nikolai Tsvetkov [†c], Bilge Yildiz [c*], and Ahmed F. Ghoniem[a*]

[a] Department of Mechanical Engineering, Massachusetts Institute of Technology, 77 Massachusetts Avenue, Cambridge, MA 02139-4307, USA

[b] Department of Mechanical Engineering, University of Alabama, Tuscaloosa, AL 35487, USA

[c] Department of Nuclear Science & Engineering, and Department of Materials Science & Engineering, Massachusetts Institute of Technology

77 Massachusetts Avenue, Cambridge, MA 02139-4307, USA

Electronic Supplementary Information

Sample characterization

Ceria and Ceria-zirconia nanopowder from Sigma Aldrich are used for the kinetics study. Table S1 lists the properties of the sample. The BET surface area is measured using a surface area and porosity analyzer (ASAP 2020 from Micrometritics). The morphology and the particle size before and after the redox treatment are characterized with a JEOL 6700 scanning electron microscopy (SEM) system. Figure S1 compares the SEM images of fresh and redox cycled samples. The fresh samples of CeO_2 and CZO contain very fine particles with the size less than

* Corresponding authors: E-mail address: ghoniem@mit.edu (Prof. Ghoniem), byildiz@mit.edu (Prof. Yildiz)
† Current address: Graduate School of Energy, Environment, Water, and Sustainability, Korea Advanced Institute of Science and Technology, Daejeon 305-701, Korea

50nm. The CeO_2 particle is slightly coarser with lower specific surface area (Table S1), and the particles clump together into a mushroom like structure with the dimension ~ 200 nm. After redox treatment, the boundaries within the clumped grain disappear: the particles sinter into larger grains forming an inter-connected structure with decreased surface area. Compared to CeO_2, the structural change and the size enlargement for CZO are less significant, resulting from the enhanced structural stability with the addition of Zr. Interesting, the variations in the measured kinetics of CeO_2 and CZO are rather small except a few initial (<5) cycles, indicating that the morphological relaxation most likely results from the sintering effect during the heating-up and initial redox cycling. Samples after additional 20 redox cycles are also examined, and the same micro-structure and redox rates are obtained, indicating that a periodic and reversible stationary equilibrium is established. Similar morphological evolutions were reported previously with H_2O splitting studies [1, 2]. The powders are confirmed as single phase by XRD analysis (Cu Ka, 45 kV and 40 mA, PANalytical X'Pert Pro Multipurpose Diffractometer, Almelo, The Netherlands) performed at room temperature in air. No change is found in the XRD patterns between the fresh and tested samples.

Table S1 Some physical properties of the CeO_2 and $Ce_{0.5}Zr_{0.5}O_2$

Property		CeO_2	$Ce_{0.5}Zr_{0.5}O_2$
Sample mass, *m*		100 mg	50 mg
Density, ρ		7.22 g cm^{-3}	6.62 g cm^{-3}
Molar density, $\tilde{\rho}_{Ce}$		4.19 $\times 10^4$ mol m^{-3}	4.50 $\times 10^4$ mol m^{-3}
Molar weight, MW		172.11 g mol^{-1}	147.66 g mol^{-1}
Surface molar density, $\tilde{\rho}_{Ce,s} = \tilde{\rho}_{Ce} a$		2.27$\times 10^{-5}$ mol m^{-2}	2.4 $\times 10^{-5}$ mol m^{-2}
fresh sample	Purity	99.95%	99.0%
	Spec. surface area, s_0	15.4 m^2 g^{-1}	38.74 m^2 g^{-1}
	Adsorption average pore width	11.2 nm	7.7 nm
	Particle size	~ 50nm	~ 24 nm
cycled sample	Spec. surface area, s_1	4.07 m^2 g^{-1}	22.96 m^2 g^{-1}
	Adsorption average pore width	8.6 nm	6.7 nm
	Particle size	~ 200nm	~ 40nm

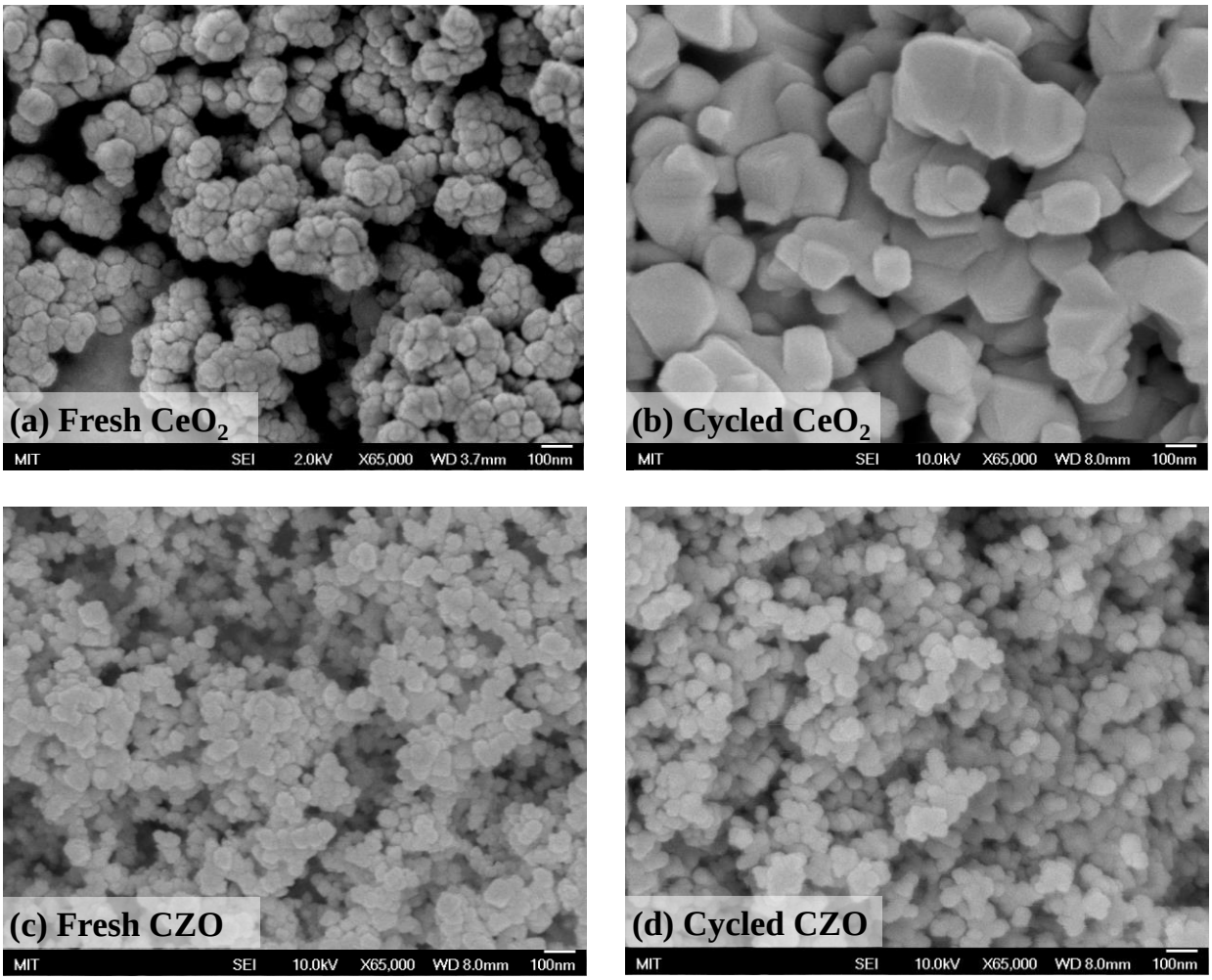

Figure S1 SEM images of the CeO_2 and CZO before redox cycles and after 50 cycles.

The measurements for CeO_2 at 1000℃ and those for CZO at 500℃ are also taken for comparison with H_2O splitting studies [1, 2]. The flue stream composition is analyzed in real-time using the QMS. The instantaneous reaction rates can be obtained as:

$$\text{CO}_2 \text{ splitting: } \omega_{ox} = \frac{X_{CO,out}\dot{n}_{ox}}{m} = \frac{X_{CO,out}}{m}\frac{P^0\dot{V}^0_{ox,in}}{RT^0} \quad (1)$$

$$\text{Reduction: } \omega_{red} = \frac{X_{H_2O,out}\dot{n}_{red}}{m} = \frac{X_{H_2O,out}}{m}\frac{P^0\dot{V}^0_{red,in}}{RT^0} \quad (2)$$

$X_{CO,\,out}$ is the measured mole fractions of the produced CO in the exit. $\dot{n}_{ox}$ and $\dot{n}_{red}$ are the total molar inflow rates of the redox gas mixture. P^0, T^0, and V^0 are the pressure, temperature, and the total volumetric inflow rate at standard temperature and pressure (STP). The reaction rates (unit, μmole $g^{-1}s^{-1}$) are normalized by the total ceria sample m, i.e., 100mg for CeO_2, and 50mg for CZO, used in the measurement.

Thus, the nonstoichiometry, i.e., the defect concentration, is calculated as

$$\delta(t) = \delta(0) - M\int_{t_0}^{t_1} \omega dt \tag{3}$$

where M is the molecular weight of CeO_2 or $Ce_{0.5}Zr_{0.5}O_2$, and $\delta(0)$ is the initial defect concentration. For the fuel reduction step, $\delta(0) = 1$, resulting from complete re-oxidation in the previous oxidation step. For the oxidation step, $\delta(0)$ is equal to the maximum non-stoichiometry achieved during the previous reduction step. See refs. 1, 3 for detailed discussion.

Non-stoichiometric defect equilibrium

Here we briefly describe the non-stoichiometric defect chemistry in the bulk phase and at the surface, following a similar approach as detailed in refs. [1, 2]. The defect formation reaction and the equilibrium mass-action relation may be written as:

$$\mathrm{O_O^\times} + 2\mathrm{Ce_{Ce}^\times} \overset{K_b}{\rightleftharpoons} \mathrm{V_O^{\bullet\bullet}} + 2\mathrm{Ce'_{Ce}} + \frac{1}{2}\mathrm{O_2}(g) \tag{4}$$

$$K_b = \exp\left(-\frac{H_b - TS_b}{RT}\right) = \frac{p_{O_2}^{1/2}\left[\mathrm{V_O^{\bullet\bullet}}\right]\left[\mathrm{Ce'_{Ce}}\right]^2}{\left[\mathrm{O_O^\times}\right]\left[\mathrm{Ce_{Ce}^\times}\right]^2} \tag{5}$$

Here the major defects are the doubly-charged oxygen vacancy, $V_O^{\bullet\bullet}$, and the localized electrons, Ce'_{Ce}, (small polarons) [4, 5]. K_b, H_b, and S_b are the equilibrium constant, enthalpy and entropy of

the defect formation reaction. The brackets denote the mole of species per mole of CeO_2 or $Ce_{0.5}Zr_{0.5}O_2$. From definition, $\left[V_O^{\bullet\bullet}\right] = \delta$, as in $CeO_{2-\delta}$ or $Ce_{0.5}Zr_{0.5}O_{2-\delta}$. Variations of K_b with the large change of δ are expected, resulting from the chemical expansion of the crystalline lattice [6, 7] as well as the defect interactions and ordering [8], leading to deviations from the ideal behavior. This effect was reported to be significant for the CZO system [9-11], which is described following a linear expression [2, 6, 9]:

$$H_b(\delta) = H_b^0(\delta = 0) + f\delta \tag{6}$$

where H_b^0 is the defect formation enthalpy for the fully oxidized CZO, and f is the δ-linear coefficient.

The transport process between the bulk and the surface enables the participation of bulk oxygen in the surface reaction. The bulk phase acts as the oxygen sink in the CO_2 splitting process or the oxygen source in the reduction step. The two-way oxygen exchange is generally governed by the defect diffusion process, described by the Nernst-Planck equation:

$$\frac{\partial C_i}{\partial t} + \frac{1}{r^2}\frac{\partial}{\partial r}\left(r^2 J_i\right) = 0 \qquad i = V_O^{\bullet\bullet}, Ce'_{Ce} \tag{7}$$

$$J_i = -\frac{C_i D_i}{RT}\frac{\partial \tilde{\mu}_i}{\partial r}, \text{ where } \tilde{\mu}_i = \mu_i^0 + RT\ln\gamma_i\frac{C_i}{C_{ref}} + z_i F\phi \tag{8}$$

where C_i, J_i, $\tilde{\mu}_i$, D_i are the defect concentration, diffusion flux, electro-chemical potential, self-diffusion coefficient. μ_i^0, γ_i, z_i are the chemical potential at reference conditions, activity coefficient, and effective charge. ϕ, T, F are the electrostatic potential, temperature, and Faraday constant. The fine nano-powder used in the kinetics study along with the fast electronic and ionic conductivities of ceria-based OCs allows for a homogeneous distribution of defect concentration

within the bulk-phase of each nano-particle. The characteristic time (τ) for diffusion from the expression $\tau \sim l^2/4D$ was estimated to be < 200 ms for CeO_2 [1] and < 1 ms for CZO [2], significantly faster than the surface chemistry. However, the defects are more stable on the surface as compared to the bulk phase (see Figure 3c), owing to the lower defect formation free energy [1, 4, 12]. The defect transport equilibrium between the surface and the bulk is described as [1, 13]:

$$\mathrm{V_O^{\bullet\bullet}}(b) - \mathrm{O_O^{\times}}(b) + 2\mathrm{Ce'_{Ce}}(b) - 2\mathrm{Ce_{Ce}^{\times}}(b) \rightleftharpoons \mathrm{V_O^{\bullet\bullet}}(s) - \mathrm{O_O^{\times}}(s) + 2\mathrm{Ce'_{Ce}}(s) - 2\mathrm{Ce_{Ce}^{\times}}(s) \quad (9)$$

$$K_T = \frac{\left[\mathrm{V_O^{\bullet\bullet}}\right]_s \left[\mathrm{Ce'_{Ce}}\right]_s^2}{\left[\mathrm{O_O^{\times}}\right]_s \left[\mathrm{Ce_{Ce}^{\times}}\right]_s^2} \Bigg/ \frac{\left[\mathrm{V_O^{\bullet\bullet}}\right]_b \left[\mathrm{Ce'_{Ce}}\right]_b^2}{\left[\mathrm{O_O^{\times}}\right]_b \left[\mathrm{Ce_{Ce}^{\times}}\right]_b^2} \quad (10)$$

The transport equilibrium constant, K_T, is expressed as, $K_T = \exp(-\Delta\mu_T / RT)$, where

$$\Delta\mu_T = \Delta H_T^0 - T\Delta S_T^0 = \left(\mu_{\mathrm{V_O^{\bullet\bullet}}}^0 + 2\mu_{\mathrm{Ce'_{Ce}}}^0\right)_{surface} - \left(\mu_{\mathrm{V_O^{\bullet\bullet}}}^0 + 2\mu_{\mathrm{Ce'_{Ce}}}^0\right)_{bulk} \quad (11)$$

Here ΔH_T^0 and ΔS_T^0 denote the difference of the defect formation enthalpy and entropy, respectively, between the surface and the bulk phase. A detailed derivation can be found in ref. [1]. The transport and defect equilibrium constant for CeO_2 and CZO are listed in Table S2.

Table S2 Parameters for the transport and bulk defect equilibria

	CeO_2 [1]	$Ce_{0.5}Zr_{0.5}O_2$ [2]
H_b^0 (kJ mol^{-1})	467.4	261.7
S_b (J mol^{-1} K^{-1})	172.9	80.1
ΔH_T^0 (kJ mol^{-1})	–107.6	–30.0
ΔS_T^0 (J mol^{-1} K^{-1})	–54.0	–9.6
f (kJ)	0	368.1

Simulation and Fitting Process

The overall governing equations for the evolutions of the surface adsorbate $\left(\mathrm{CO_3}\right)_{\mathrm{O}}^{\cdot\cdot}$ and the bulk-phase $\mathrm{V_O^{\cdot\cdot}}$ are [1]:

$$\tilde{\rho}_s \frac{d\left[\left(\mathrm{CO_3}\right)_{\mathrm{O}}^{\cdot\cdot}\right]_s}{dt} = \tilde{\rho}_s\left(r_1 - r_2\right) \tag{12}$$

$$\frac{d}{dt}\left(\tilde{\rho} V_R \left[V_O^{\bullet\bullet}\right]_b\right) = -S_R \tilde{\rho}_{Ce,s} r_1 \tag{13}$$

where $\tilde{\rho}_s$, $\tilde{\rho}$ are the surface and the bulk molar density of the unit cell. V_{R}, and S_{R} are the volume and the surface area of the particle. The conservation equations for the surface are:

O-site: $$\left[\mathrm{V_O^{\cdot\cdot}}\right]_s + 2\left[\left(\mathrm{CO_3}\right)_{\mathrm{O}}^{\cdot\cdot}\right]_s + \left[\mathrm{O_O^{\times}}\right]_s = 2 \tag{14}$$

Ce-site: $$\left[\mathrm{Ce'_{Ce}}\right]_s + \left[\mathrm{Ce_{Ce}^{\times}}\right]_s = 1 \text{ (for } \mathrm{CeO_2}\text{) or } 0.5 \text{ (for CZO)} \tag{15}$$

electro-neutrality $$2\left[\mathrm{V_O^{\cdot\cdot}}\right]_s + 2\left[\left(\mathrm{CO_3}\right)_{\mathrm{O}}^{\cdot\cdot}\right]_s = \left[\mathrm{Ce'_{Ce}}\right]_s \tag{16}$$

The surface electro-neutrality is assumed based on the conclusions from previous work on ceria [1, 2, 14] as well as other materials [15].

Governing equations are numerically integrated in MATLAB. The kinetic parameters to be obtained are $k_{1,\mathrm{b}}$, $k_{2,\mathrm{b}}$, K_2, with the other kinetic parameters obtained via equilibrium relations. The variation of H_{b} with δ from eq. **(6)** for CZO is assumed to be associated with the oxygen removal step ($k_{1,\mathrm{b}}$ for backward R1) [2]. Thus, $E_{1,b} = E_{1,b}^0 + f\delta$, where f corresponds to eq. (6). With the time-resolved profiles of $[\mathrm{CO_2}]$ using the QMS, the entire conversion process can be predicted based on a given set of kinetic parameters. The predicted CO production profile is then compared to the measurements, and the kinetics parameters are varied to minimize the difference:

$$Diff = \sum_{all\ tests} \sqrt{\frac{1}{N} \sum_{0 \le t \le t^*} \left(\hat{\omega}_{\text{model}} - \hat{\omega}_{\text{measure}} \right)^2} \tag{17}$$

Here the reaction rates ($\hat{\omega}_{\text{model}}$ or $\hat{\omega}_{\text{measure}}$) are normalized by the maximum rate, and N is the number of measurement points in each test. The minimization is obtained numerically in MATLAB using fminsearch solver[16].

Specific Surface Kinetics

As discussed in the manuscript, the addition of Zr in CZO promotes the structural resistance to thermal and redox treatment, maintaining a higher surface area as compared to CeO_2 ($s_{1,\,CZO} \approx 5.6\ s_{1,\,CeO2}$, see Table S1), which favors the surface splitting kinetics. On the other hand, structurally inert Zr^{4+} ions relaxes the bond strength, alters the reaction attempt frequencies, thus affecting the kinetics and energy landscape of the splitting pathway. To elucidate the chemical effect of Zr^{4+}, we plot the measured surface specific CO_2 splitting rates in Figure S2. The peak rate is normalized by the specific surface area as listed in Table S1, and hence the contribution of the surface area difference is excluded. Above 800°C, the specific splitting rate is significantly higher for CeO_2 as compared to CZO, which results from much higher [CO_3^{2-}] and [Ce^{3+}]. The trend, however, is reversed at lower temperature, caused by the lower defact formation enthalpy of CZO (hence promoting surface defects concentration), as well as the lower activation barrier for the charge-transfer step.

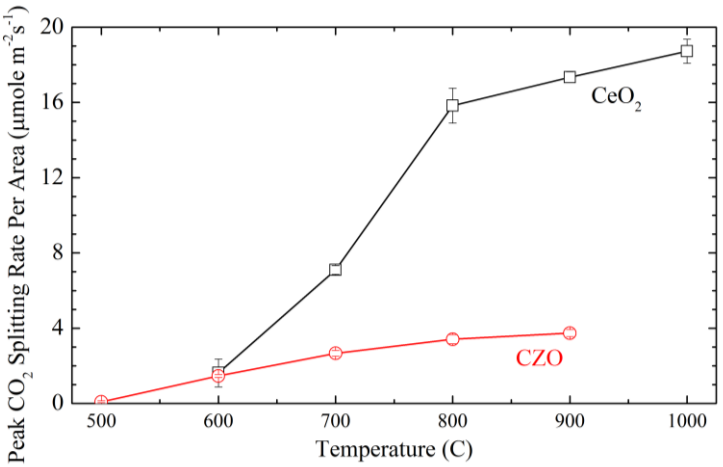

Figure S2 Comparison of peak CO_2 splitting kinetics, normalized by sample specific surface area.

Figure S3 further breaks down the splitting kinetics following the two-step reactions, and compares the effect of Zr on the reaction rate of each step. In panel (a), R1 forward (adsorption) reaction for CeO_2 is an order of magnitude faster compared to CZO, consistent with the much higher $k_{1,f}$ as listed in Table 2. R1 backward (defect formation) reaction shows a similar discrepency, which is attributed to the higher surface $[CO_3^{2-}]$ for CeO_2 compensated by a lower $k_{1,b}$. R2 forward (charge transfer) step accounts for the difference of the CO_2 splitting rate observed in Figure S2: it shows an combined effect (eq. 7) from surface defects ($[Ce^{3+}]_{CeO2} \approx 2\,[Ce^{3+}]_{CZO}$, see Figure 4), adsorbates ($[CO_3^{2-}]_{CeO2} \approx 50\,[CO_3^{2-}]_{CZO}$, see Figure 8), and reaction dynamics ($k_{2,f\ CeO2} \approx 0.03\,k_{2,f\ CZO}$, see Table 2). The reverse of the trend showed in panel (b) can be explained similarly. Both forward and backward reaction rates of R1 for CZO become remarkably faster, while the charge transfer step (R2 forward) at 600℃ becomes comparable between CZO and CeO_2.

The comparison here highlights the key characteristics of Zr: on one hand, the addition of inert Zr^{4+} limits oxygen carrying capacity and restricts the surface preferable adsorption sites, which lowers the surface defect and adsorbate concentration, and hence negatively impacts the splitting kinetics at high temperature; on the other hand, the relaxed crystal structures along with lowered defect formation enthalpy and charge transfer barrier promotes the splitting kinetics at lower temperature. These properties, coupled with the higher surface areas, enables CZO as a promising OC candidate for intermediate-low temperature CO_2 splitting.

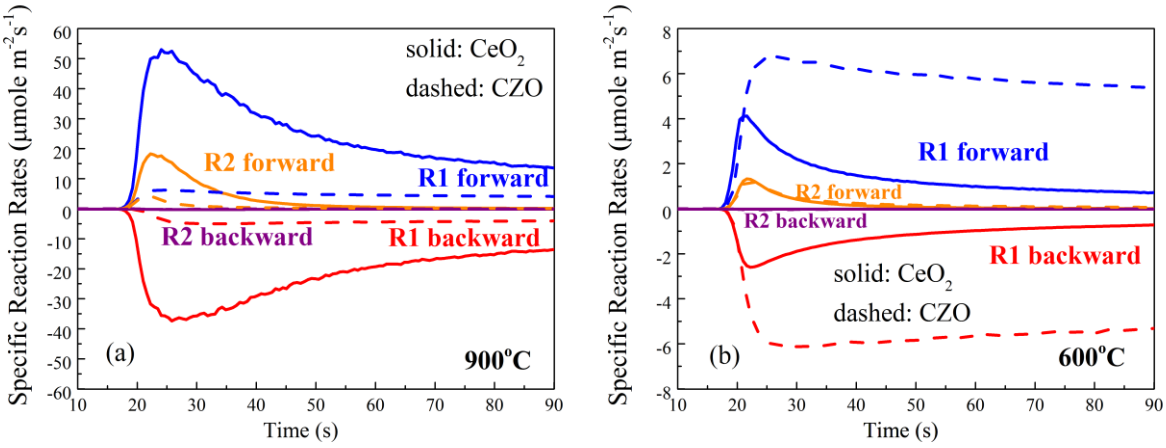

Figure S3 Comparison of the surface specific reaction rates, normalized by specific surface area, at 900℃ and 600℃ for CeO_2 (solid lines) and CZO (dashed lines). Backward reactions are plotted as negative values for clarity.

Reference

1. Z. Zhao, M. Uddi, N. Tsvetkov, B. Yildiz and A. F. Ghoniem, *J. Phys. Chem. C*, 2016, 120, 16271-16289.
2. Z. Zhao, M. Uddi, N. Tsvetkov, B. Yildiz and A. F. Ghoniem, *J. Phys. Chem. C*, 2017, DOI: 10.1021/acs.jpcc.1027b00644.
3. Z. Zhao, Massachusetts Institute of Technology, 2016.
4. W. C. Chueh, A. H. McDaniel, M. E. Grass, Y. Hao, N. Jabeen, Z. Liu, S. M. Haile, K. F. McCarty, H. Bluhm and F. El Gabaly, *Chem. Mater.*, 2012, 24, 1876-1882.
5. M. Mogensen, N. M. Sammes and G. A. Tompsett, *Solid State Ionics*, 2000, 129, 63-94.

6. S. R. Bishop, T. S. Stefanik and H. L. Tuller, *Phys. Chem. Chem. Phys.*, 2011, 13, 10165-10173.
7. C. Chatzichristodoulou and P. V. Hendriksen, *J. Electrochem. Soc.*, 2010, 157, B481-B489.
8. H. Tuller and A. Nowick, *J. Electrochem. Soc.*, 1979, 126, 209-217.
9. D. Chen, Y. Cao, D. Weng and H. L. Tuller, *Chem. Mater.*, 2014, 26, 5143-5150.
10. G. Zhou, P. R. Shah, T. Kim, P. Fornasiero and R. J. Gorte, *Catal. Today*, 2007, 123, 86-93.
11. M. Kuhn, S. R. Bishop, J. L. M. Rupp and H. L. Tuller, *Acta Mater.*, 2013, 61, 4277-4288.
12. T. Sayle, S. Parker and C. Catlow, *Surf. Sci.*, 1994, 316, 329-336.
13. J. Maier, *Physical chemistry of ionic materials: ions and electrons in solids*, John Wiley & Sons, 2004.
14. Z. A. Feng, F. El Gabaly, X. Ye, Z.-X. Shen and W. C. Chueh, *Nat Commun*, 2014, 5.
15. G. Dimitrakopoulos and A. F. Ghoniem, *Journal of Membrane Science*.
16. J. C. Lagarias, J. A. Reeds, M. H. Wright and P. E. Wright, *SIAM Journal on optimization*, 1998, 9, 112-147.